Supplementary Information for

A semi-vapor electrolysis technology for hydrogen generation from wide water resources

Authors: Jiayi Tang[1], Ke Guo[2, 3], Daqin Guan[1], Yong Hao[3, 4], and Zongping Shao[1*]

[1]WA School of Mines: Minerals, Energy and Chemical Engineering (WASM–MECE), Curtin University, Perth WA 6102, Australia.

[2]Department of Thermal Science and Energy Engineering, University of Science and Technology of China, Hefei 230027, China.

[3]Institute of Engineering Thermophysics, Chinese Academy of Sciences, Beijing 100190, China.

[4]University of Chinese Academy of Sciences, Beijing 100049, China.

* Corresponding author. Email: zongping.shao@curtin.edu.au

This PDF file includes:

Experimental section

Preparation of catalyst coated membrane (CCM)

Nafion™ NR212 was bought from Chemours and used as received. Perfluorinated resin solution containing Nafion™ 1100W (5 wt.% in ethanol) was bought from Sigma-Aldrich. First, the anode catalyst layer was formed onto the PEM by spraying coating. Ruthenium (IV) oxide (RuO_2, Sigma-Aldrich, 99.9 % trace metals basis) or core/shell Ir/IrO_x catalyst (Fuel Cell Store) was mixed with ionomer at a weight ratio of 8-16 wt.% and fully dispersed in solvent (water: isopropyl alcohol = 1: 2, v/v) in an ultrasonic water bath for 1 h to prepare the anode catalyst ink, during which the temperature was controlled at constant 25 ℃. The catalyst ink was used immediately after preparation. Spraying coating was performed manually by a spray gun (TAIWAN, HD-131, 0.2 mm caliber). An active area of 2 × 2 cm^2 or 5 × 5 cm^2 was demarcated on the NR212 membrane to be sprayed with the as-formed anode catalyst ink. The spray rate and the base temperature was controlled to allow immediate evaporation of the solvent to form uniform catalyst layers. The cathode catalyst layer was then prepared following the similar procedures. Platinum carbon catalyst (Pt/C, 60 wt.% on EC-300J, Fuel Cell Store) was mixed with the same ionomer at an ionomer to carbon ratio (I/C) of 60 wt.% and solvent (water: ethanol = 1: 1, v/v) to form the uniform catalyst ink, which was then sprayed onto the corresponding area on the other side of the membrane. The CCM was ready to use after being hot-pressed under 100 psi at 135 ℃ for 60 s. The catalyst loadings for both sides were determined by weighing the weight gain after spraying and drying in trial productions with the margin of error < 0.1 mg cm^{-2}.

Electrolyzer fabrication

The electrolyzer was made of pure titanium (Ti) and was customized with the anode and cathode plates engraved with parallel flow field. Platinized Ti fiber felt (~265 μm, Fuel Cell Store) was used as the anode gas diffusion layer (GDL), and carbon paper (~280 μm, Toray-TGP-H-090) was used as the cathode GDL. Polytetrafluoroethylene (PTFE) films were equipped with the GDLs for anode and cathode chamber sealing and to achieve an appropriate carbon paper compression rate of 25% in electrolyzer assembly. To enable fully contact of the components in electrolyzer, an assembly force of 2.5 Nm was applied to the fasten bolts of the 2 × 2 cm^2 single electrolyzer unit, and 3.5 Nm to the 5 × 5 cm^2 electrolyzer stack.

SVE system setup

For operating the electrolyzer under SVE mode, saturated vapor generated at dew points of 60–95 ℃ through a bubbling-enhanced vaporization process was carried by gas (nitrogen,

oxygen, or air) at a constant flow rate of 200 mL $min^{-1}_{[STP]}$, and fed to the anode of the electrolyzer. The water sources for generating vapor were collected in Western Australia, including seawater from Indian Ocean, lake water from Lake Monger (Perth), river water from Swan River (Perth), rainwater, and tap water. The diagram and detailed operation of the vapor vessel for vapor generation and supply are presented in **Fig. S2**. During the operation of the SVE, DI water heated up to 90 °C was circulated at 80 mL min^{-1} to maintain a constant temperature of the electrolyzer and keep the membrane hydrated during the operation. For operating the electrolyzer under WLE mode, DI water was heated up to 90 °C and circulated at 80 mL min^{-1} at the anode and the cathode side individually. Other operating conditions were used as controls, for example, the full-vapor mode by supplying the anode and the cathode with saturated vapor under designated temperature individually at 200 mL $min^{-1}_{[STP]}$, or the An-vapor mode by only supplying vapor to the anode while leaving the cathode free from any form of water supply. The performance curves obtained for SVEs and WLEs are presented as tested without iR correction.

Characterizations

The ion conductivity test was performed on a SmartCHEM-LAB instrument (TPS) equipped with a glass conductivity sensor (k = 0.1) and a temperature sensor. Each liquid sample was tested for 3 times under temperature control and take the average value. Inductively coupled plasma optical emission spectroscopy (ICP-OES) measurements were conducted on PerkinElmer Optima 8300 to study the possible dissolution of the RuO_2 catalyst during stability test. The in-plane electronic conductivity of the anode catalyst layer was measured under both vapor atmosphere of different RH and in water liquid by Van der Pauw (VDP) method,[1] and was calculated as follows:

$$\exp\left(\frac{-\pi R_{AB}}{R_S}\right) + \exp\left(\frac{-\pi R_{AC}}{R_S}\right) = 1$$

$$\sigma_{IP} = {}^{1}/_{R_s t}$$

where R_{AB} and R_{AC} are the resistances measured in two perpendicular directions of the catalyst layer sample placed under different conditions. R_s as obtained is defined as the sheet resistance of the catalyst layer. t is the thickness of the catalyst layer.

Electrolyzer performance tests

Electrolyzer performance tests were conducted on a programmable power supply of Keysight (E36233A, 200 W). The electrolyzer was placed in a thermal-insulating jacket to reduce the influence of environmental temperature changes and keep the temperature constant during the

measurements. Before recording the polarization curves, activation of the electrodes was performed by running stepwise at small current densities of 100 mA cm^{-2}, 200 mA cm^{-2}, and 400 mA cm^{-2} for 10 min at each point. Then the polarization curves were measured by stepping the voltage from 1.2 V to 1.8 V with an increment of 10 mV, and each voltage point was held for 30 s to record the stabilized electrolysis current. The performance was tested for 3 times and the average value of each measured point was used. The stability tests were conducted by applying a constant current density of 0.2 A cm^{-2}, 1.0 A cm^{-2} or 2.0 A cm^{-2} to the electrolyzer and the voltage changes over time were recorded. EIS measurements were performed on a Gamry Reference 3000 under both galvanostatic mode and potentiostat mode. For running under galvanostatic mode, at specific operating current densities, an AC perturbation of 10% of the DC current was applied, and the responses of impedance were recorded from 10 kHz to 100 mHz. For running under potentiostat mode, an AC oscillation of 10 mV amplitude at 0 V was applied over the frequencies from 10 kHz to 100 mHz. Data points presented are averages of two times measurement for per decade.

Energy consumption and efficiency calculations

The energy consumption and efficiency were calculated based on the electrolyzer itself not including the BoP. The mass of H_2 (m_{H_2}, kg) got produced under apparent current density J (A cm^{-2}) for certain time t (s) can be calculated via the following equation:

$$m_{H_2} = M_{H_2} \times J \cdot A \cdot t/(n \cdot F \cdot 1000)$$

n is the number of electrons transferred for H_2 production, A (cm^2) is the active area of the electrode, M_{H_2} is the molar mass of H_2, F is the Faradic constant, which is 96,485 C mol^{-1}. Energy consumption W_e (kWh kg^{-1}) of specific mass of hydrogen at applied voltage V (V) was thus calculated as follows,

$$W_e = I \cdot \int V dt / m_{H_2}$$

where I is the current. Considering the lower heating energy (LHV) of hydrogen is 33.0 kWh kg^{-1}, thus the energy efficiency ($LHV\%$) was calculated as:

$$LHV\% = 33.0/W_e$$

Thermodynamic calculations

The thermodynamic equilibrium potentials or thermoneutral voltages for H_2 production from water liquid and water vapor electrolysis were calculated from the enthalpy changes ($\Delta_f H$) as expressed below,

$$\Delta_f H[H_2O(l), T] = \Delta G[H_2O(l), T] + T\Delta S_l$$
$$\Delta_f H[H_2O(g), T] = \Delta G[H_2O(g), T] + T\Delta S_g$$

The enthalpy change ($^{\Delta_f H}$) of water electrolysis consists of the Gibbs free energy change (ΔG), which decides the reversable voltage required for the onset of water electrolysis reaction, and the reversible heat $T\Delta S$ associated with the entropy change of the reaction. The sum of the two determines the net energy required for the water electrolysis to take place. The thermochemistry data for calculating the reaction enthalpy changes at different temperatures was obtained from NIST Standard Reference Data.[2, 3] For water liquid electrolysis, the entropy change ($^{\Delta S_l}$) during the reaction includes the transformation of liquid water to gaseous water and the volume expansion from gaseous water reactant to hydrogen gas and oxygen gas products as follows, while for water vapor electrolysis, the entropy change ($^{\Delta S_g}$) is theoretically associated only with the second step of volume expansion.

$$H_2O\ (l) \rightarrow H_2O\ (g)$$
$$H_2O\ (g) \rightarrow H_2\ (g) + \frac{1}{2}O_2(g)$$

According to the Nernst Equation as shown below, the thermodynamic equilibrium potentials (U_{th}) of water liquid and water vapor electrolysis were calculated, and the obtained values and calculation details are presented in **Supplementary Discussion #1 and Tab. S5, 6**.

$$U_{th} = \Delta_f H[H_2O, T]/nF$$

During the reaction at voltages (U_{cell}) higher than U_{th}, the electrolysis heat dissipation associated with the irreversible processes can be calculated by the following equation:

$$Q_{ex} = nF \cdot (U_{cell} - U_{th})$$

The energy required for vaporization process is the sum of energy for water source heat up to designated temperature and the energy for water phase transition at that temperature.

Techno-economic analysis

Commercial PEMWE hydrogen production cost was used as a baseline. The assessments of cost breakdown factors and the calculations of cost reduction were performed to evaluate the projected hydrogen production cost through the SVE. The referenced case of distributed PEMWE was the Hydrogen Production Analysis model, version 3.2018 (H2A v3.2018),[4] where a thorough bottom-up economic analysis and rigorous data scrutiny was performed to ensure the accuracy of the calculated results. Following the case study, the techno-economic analysis of hydrogen production from the PEM-based SVE in this work demonstrates a

relatively high level of reliability. The primary factors contributing to the cost reduction through the SVE include the reduced electricity consumption with improved efficiency, the replacement of electrode material, the deductions from water purification requirements, and the revenue brought by the by-products during green hydrogen production. We individually calculated the cost reductions from these four aspects. Detailed input parameters and calculations are presented in **Supplementary Discussion #2 and Tab. S7, 8**.

The tornado chart developed employs univariate sensitivity to examine the impact of individual parameters on hydrogen production cost. The Y-axis denotes different single input parameters, while the X-axis quantifies the anticipated variations. Crucial variables scrutinized for their influence on hydrogen production costs encompass (1) average electricity price; (2) electricity usage; (3) stack costs; (4) BoP costs; (5) installation cost; and (6) replacement costs. The numerical values situated at the extremities of the graph signify the spectrum of change in input parameters. The graphical representation, employing a color-coded scheme, vividly illustrates the resulting escalation (highlighted in red) or reduction (emphasized in dark green) in the baseline cost of hydrogen production due to the modifications of the input parameters.

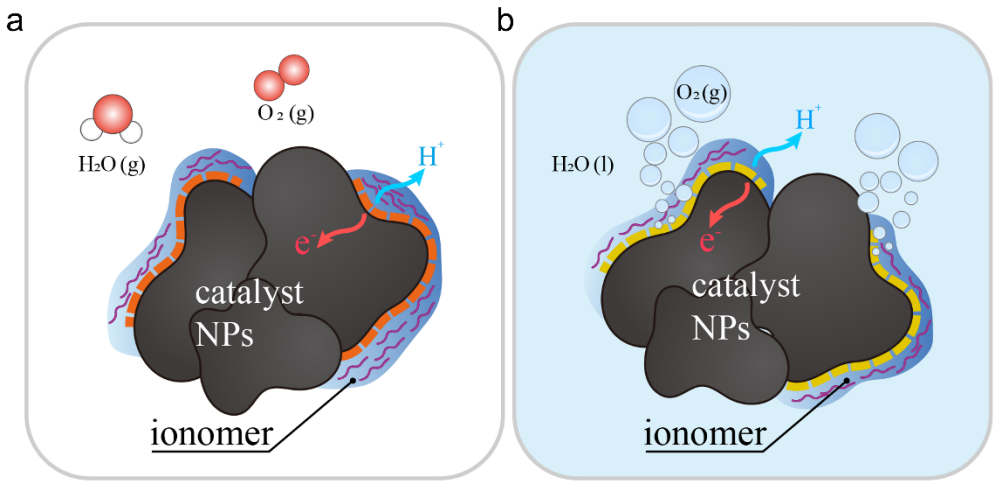

Fig. S1 Schematic illustration of the single-phase reaction involved in **a**, water vapor electrolysis, and the two-phase reaction involved in **b**, water liquid electrolysis.

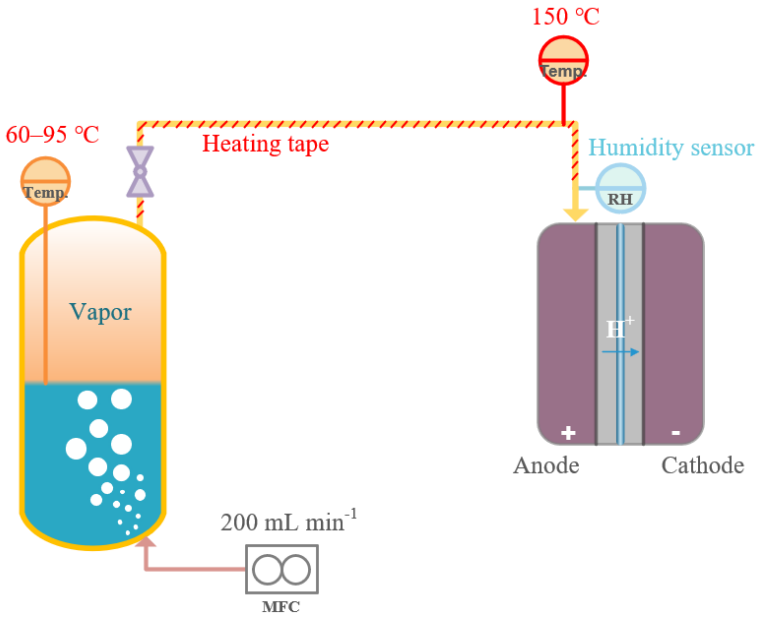

Fig. S2 Schematic illustration of vapor generation and supply under conditions control.

The bubbling-enhanced vaporization and vapor supply process is illustrated in **Fig. S2**. Half of the vapor vessel was filled with raw water, and the volume was controlled by a liquid level gauge. The water inside the vessel was heated to a certain temperature between 60 to 95 °C by the heating element built in the vessel, and the vessel was fully insulated by a heating jacket to keep the temperature, so that the vapor generation under the control of the dew point will not condense on the top of the vessel. Several other parameters were controlled to get saturated or near saturated vapor supply at the anode inlet. The carrier gas was injected in from the bottom of the vessel and controlled at a constant rate of 200 mL $min^{-1}_{[STP]}$ by a mass flow controller (MFC) and was fine-bubbled through a micro-ceramic gas diffuser. The extended gas-liquid interface created by the refined bubbling process was able to greatly increase the vaporization rate, thus, to ensure saturated vapor supply even under relatively high gas flow rates. The pipeline for transporting vapor to the electrolyzer was kept at around 150 °C with a wrapped heating tape to ensure that vapor can be supplied to the anode inlet of the electrolyzer without condensation.

Tab. S1 Thermodynamic parameters and process for hydrogen production dealing with water liquid and water vapor electrolysis.

Parameters	Water liquid electrolysis	Water vapor electrolysis

Overall reaction	$H_2O(l) + \Delta_f H^0[H_2O(l), T] \rightarrow H_2(g$ (g)	$H_2O(g) + \Delta_f H^0[H_2O(g), T] \rightarrow H_2(g$ (g)
Enthalpy change ($\Delta_f H^0$)	$\Delta_f H^0[H_2O(l), T] = \Delta G^0[H_2O, T] +$	$\Delta_f H^0[H_2O(g), T] = \Delta G^0[H_2O, T] +$
Entropy change (ΔS)	$H_2O\ (l) \rightarrow H_2O\ (g)$ * $H_2O\ (g) \rightarrow H_2\ (g) + \frac{1}{2}O_2(g)$	$H_2O\ (g) \rightarrow H_2\ (g) + \frac{1}{2}O_2(g)$

Tab. S2 Relative humidity and temperature detected at the anode inlet.

Vapor vessel temperature (°C)	Heating tape temperature (°C)	Relative humidity (%)	Inlet feedstock temperature (°C)
65	150	91.7	66
70	150	94.1	73
80	150	97.4	79
90	150	98.0	87

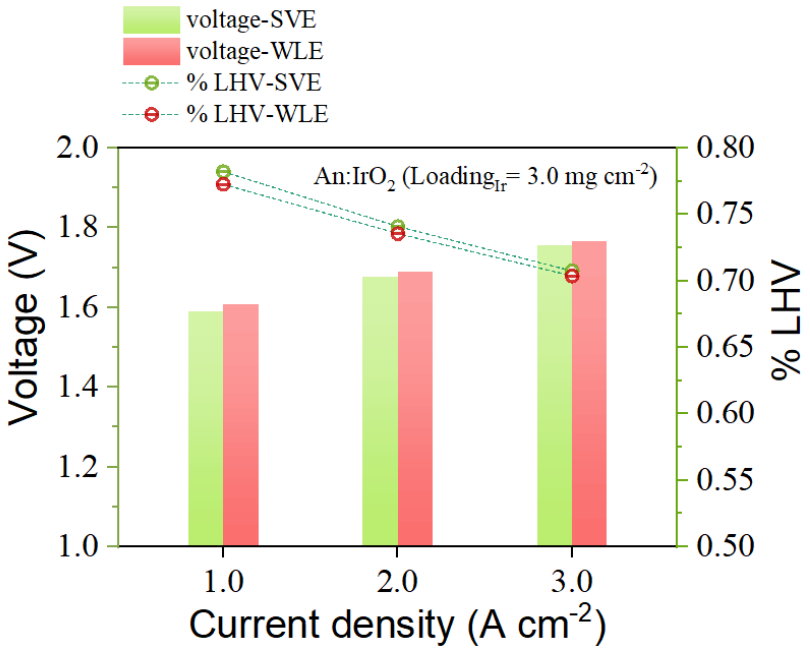

Fig. S3 Comparison of voltage and efficiency by running the electrolyzer at different current densities under semi-vapor mode (labelled as SVE) and conventional water-liquid mode (labelled as WLE). IrO_2 is used as the anode catalyst at an Ir loading of 3.0 mg cm^{-2}.

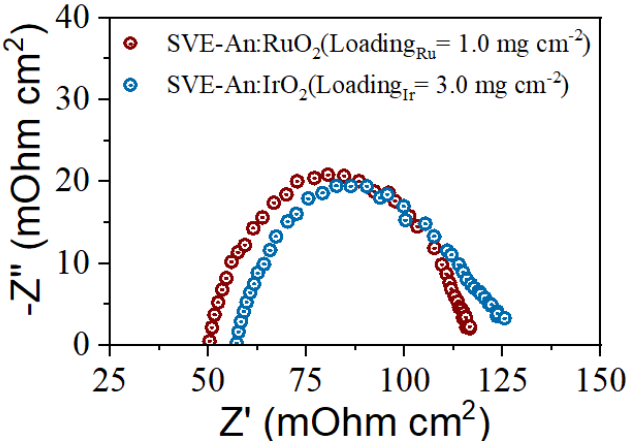

Fig. S4 Nyquist plots obtained from galvanostatic EIS measurements of the 2 × 2 cm^2 electrolyzer in operation at 2.5 A applied current under the SVE (Anode feed: saturated vapor at 90 °C carried by N_2 gas at 200 mL min^{-1}, cathode feed: 90 °C pure water at 80 mL min^{-1}, and the electrolyzer temperature was kept at 90 °C).

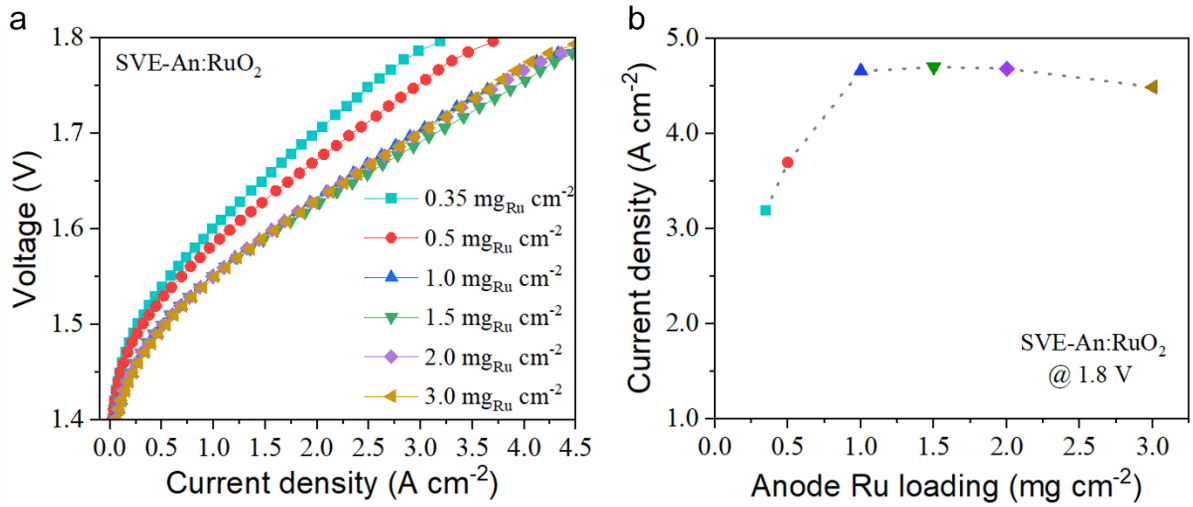

Fig. S5 a, Polarization curves of the SVEs with different Ru loadings from 0.35 to 3.0 mg_{Ru} cm^{-2} in the anodes. **b**, A comparison of the electrolysis current densities achieved at 1.8 V with different Ru loadings. (2 × 2 cm^2 electrolyzer single cell, anode feed: saturated vapor at 90 °C carried by N_2 gas at 200 mL min^{-1}, cathode feed: 90 °C pure water at 80 mL min^{-1}, and the electrolyzer temperature was kept at 90 °C).

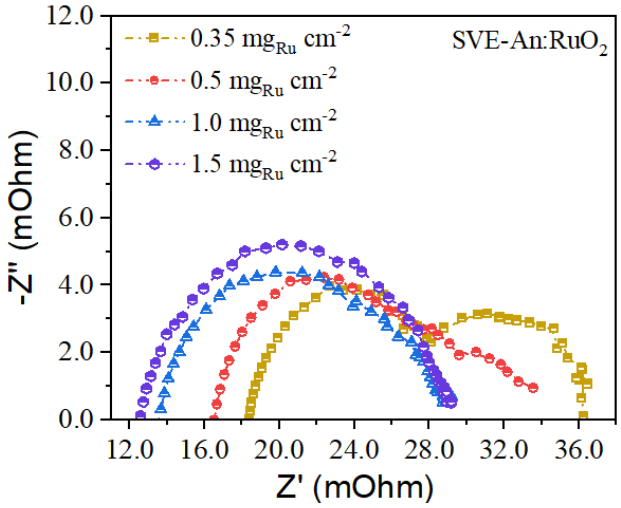

Fig. S6 Nyquist plots obtained from galvanostatic EIS measurements of the 2 × 2 cm^2 SVEs in operation at 2.5 A applied current fabricated with RuO_2 anodes at different Ru loadings. (Besides the reduced charge transfer resistance, as the Ru loading increases from 0.35 to 1.5 mg cm^{-2}, the ohmic resistance was found to gradually decrease. This may be due to the increased thickness of the anode catalyst layer, which compensates for the electronic conductivity of the anode layer itself and the contact between the anode and the Ti diffusion layer.)

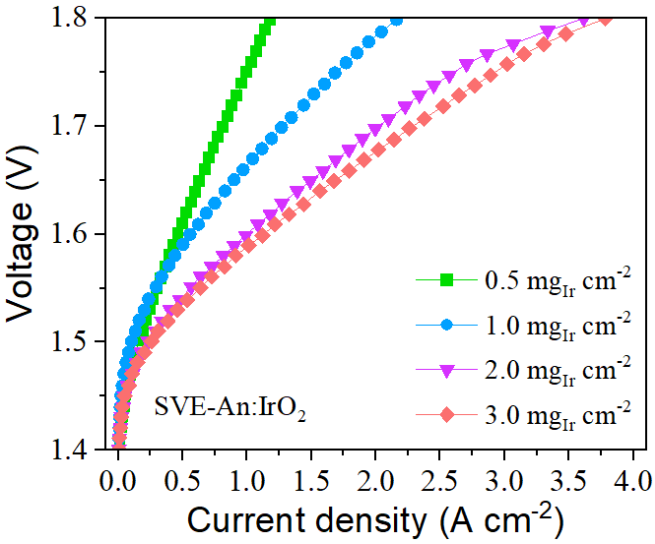

Fig. S7 Polarization curves of the SVEs with different Ir loadings from 0.5 to 3.0 mg_{Ir} cm^{-2} in the anodes.

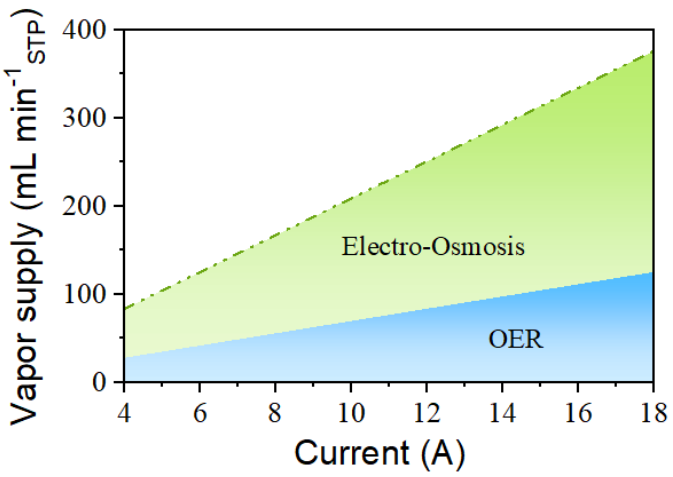

Fig. S8 Required vapor supply for electro-osmosis and OER processes as a function of electrolysis current.

Tab. S3 Saturated vapor pressure at different temperature

Temperature (℃)	Saturated vapor pressure (Pa)
65	24767.76
70	30866.16
80	46925.25
90	69485.08
95	83783.71

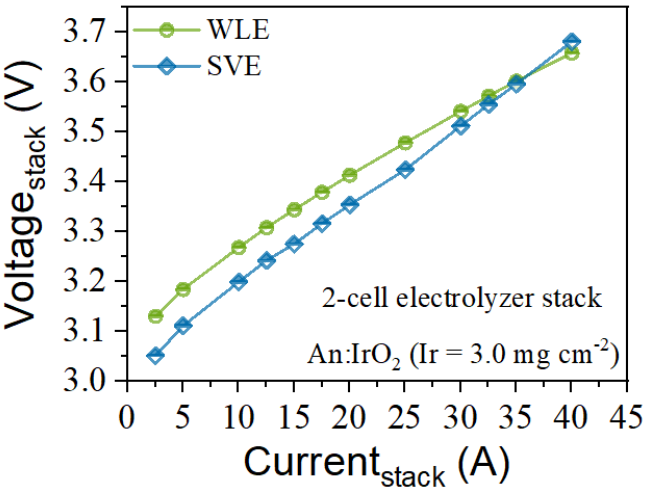

Fig. S9 Performance curves of the 2-cell SVE stack and the WLE stack fabricated with IrO_2-based anode at an Ir loading of 3.0 mg cm^{-2}. (For the SVE stack, the anode is supplied with

60 ℃ vapor and the cathode is circulated with 60 ℃ DI water; for the WLE stack, both the anode and the cathode are supplied with 60 ℃ DI water.)

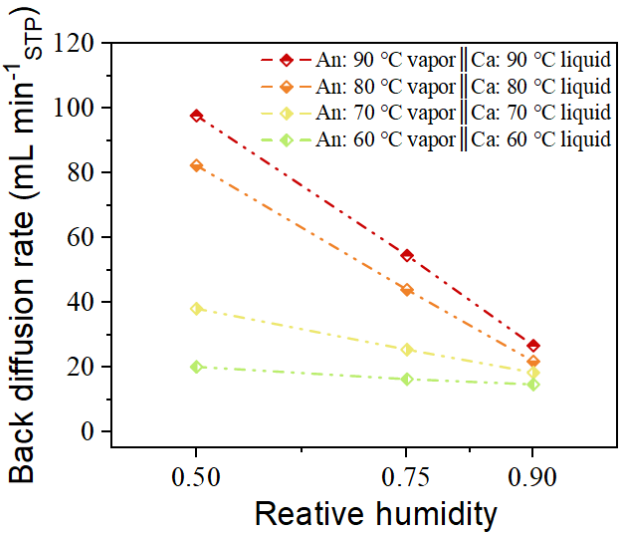

Fig. S10 Water back diffusion rate measured under static SVE conditions. The anode is maintained with humidified gas atmosphere, and the relative humidity is controlled by controlling the partial vapor pressure from vapor generation (as shown below in **Tab. S4**). The vapor inlet as well as the electrolyzer temperature are controlled by an external water bath. The cathode is circulated with pure water at certain temperatures. The back diffusion rate is obtained by measuring the water decrease at the cathode side over a period of time. *The data show the rough trend of back diffusion rate as a function of relative humidity; however, it should be noted that the results obtained under high humidity may be inaccurate due to the difficulty for precisely controlling the partial vapor pressure.

Tab. S4 The vapor generation temperature and anode inlet temperature controlled to obtain specific relative humidity for static SVEs conditions.

Relative humidity	0.5	0.75	0.9	Inlet temperature (℃)
Vapor generation temperature (℃)	45.8	53.9	57.7	60
	54.8	63.5	67.6	70
	63.8	73.1	77.4	80
	72.7	82.6	87.3	90
	77.2	87.4	92.2	95

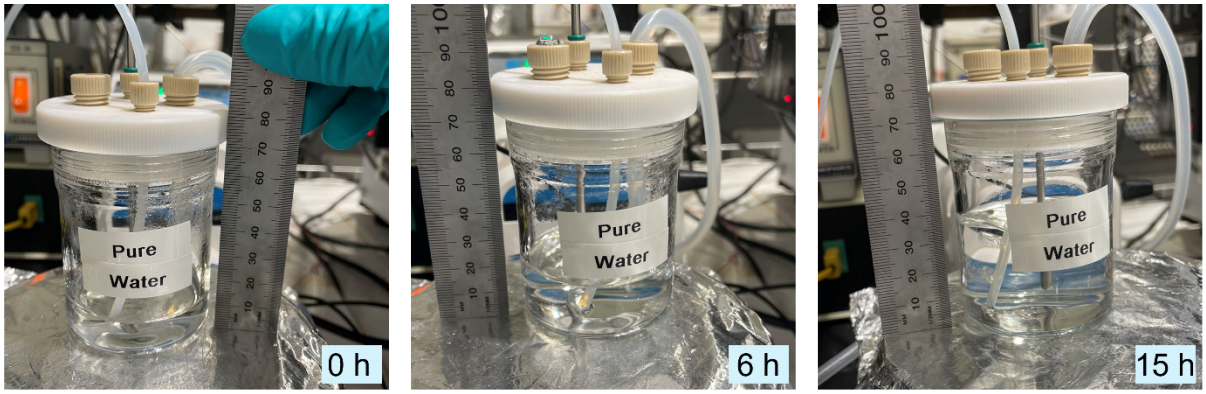

Fig. S11 The cathode water increase observed with sufficient vapor supply at the anode side after a period time of operation. The SVE is operated under 1.0 A cm^{-2}.

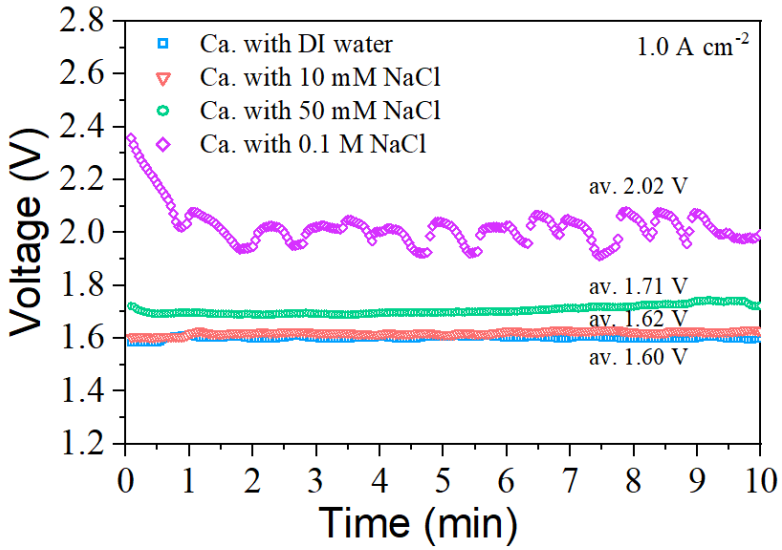

Fig. S12 Voltages required for delivering an electrolysis current density of 1.0 A cm^{-2} under the SVE operation by substituting the cathode circulation with NaCl solution at different concentrations compared to that with DI water.

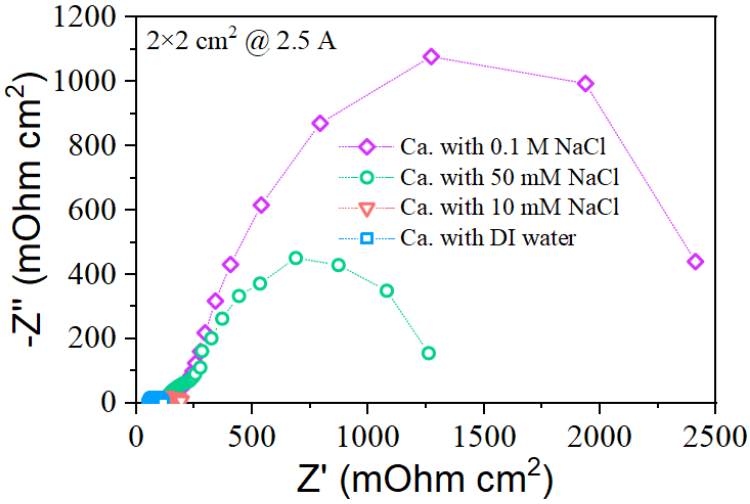

Fig. S13 Nyquist plots obtained from galvanostatic EIS measurements of the 2 × 2 cm^2 SVEs in operation at 2.5 A applied current with the cathode supplied by NaCl solution at different concentrations and DI water.

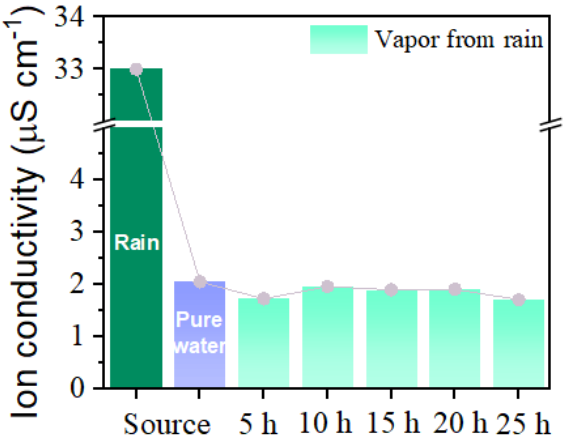

Fig. S14 The ion conductivity of the vapor condensate collected during a 25-h bubbling enhanced vaporization process from rainwater.

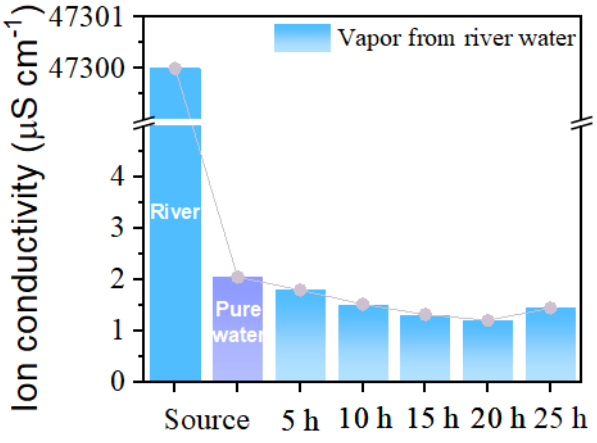

Fig. S15 The ion conductivity of the vapor condensate collected during a 25-h bubbling enhanced vaporization process from river water.

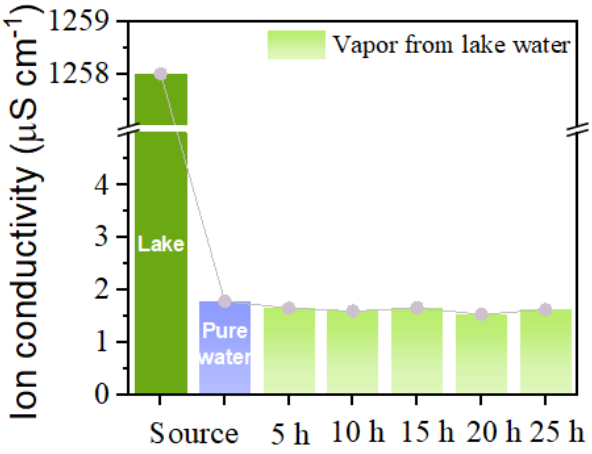

Fig. S16 The ion conductivity of the vapor condensate collected during a 25-h bubbling enhanced vaporization process from lake water.

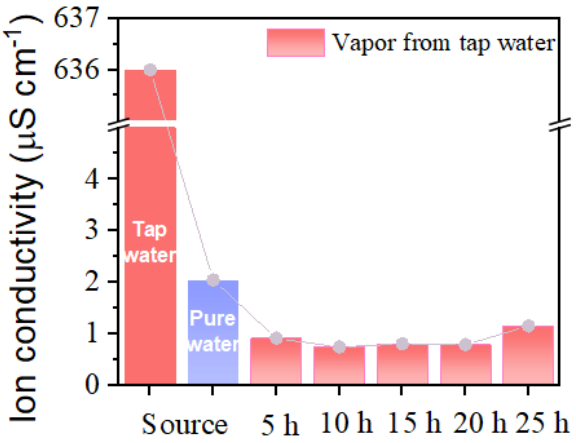

Fig. S17 The ion conductivity of the vapor condensate collected during a 25-h bubbling enhanced vaporization process from tap water.

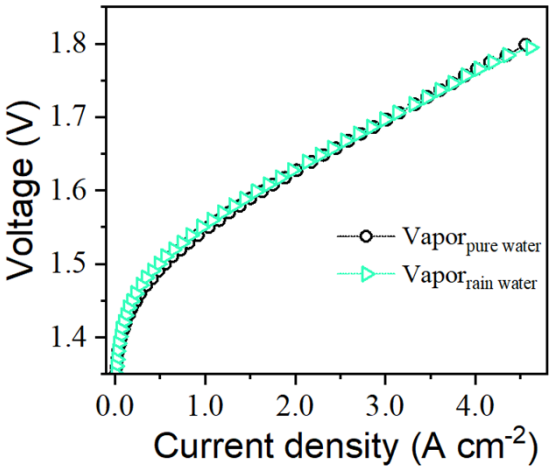

Fig. S18 SVE performance with vapor generated from pure water and rainwater respectively. (2 × 2 cm^2 electrolyzer single cell, anode feed: saturated vapor at 90 ℃ carried by N_2 gas at 200 mL min^{-1}, cathode feed: 90 ℃ pure water at 80 mL min^{-1}, and the electrolyzer temperature was kept at 90 ℃)

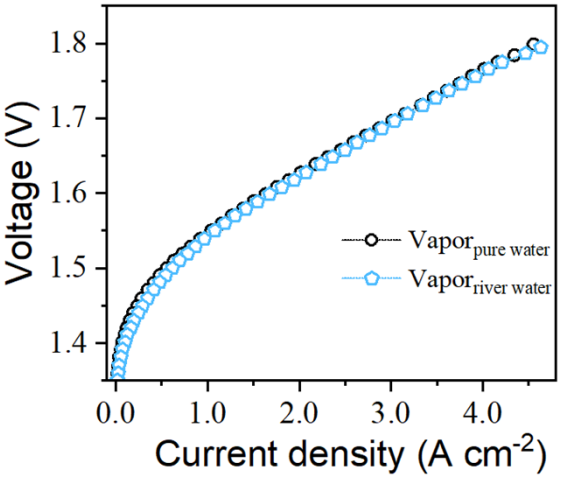

Fig. S19 SVE performance with vapor generated from pure water and river water respectively.

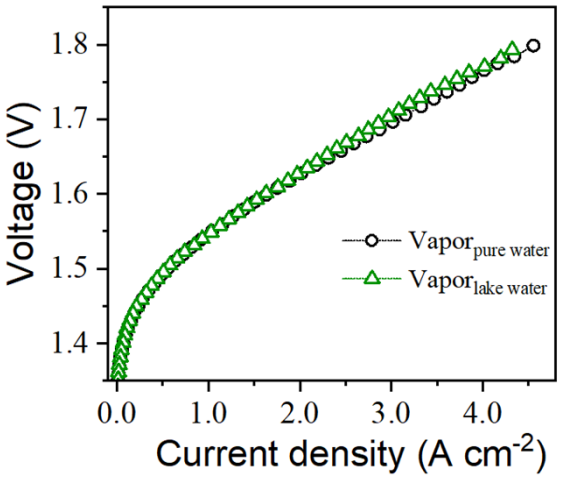

Fig. S20 SVE performance with vapor generated from pure water and lake water respectively.

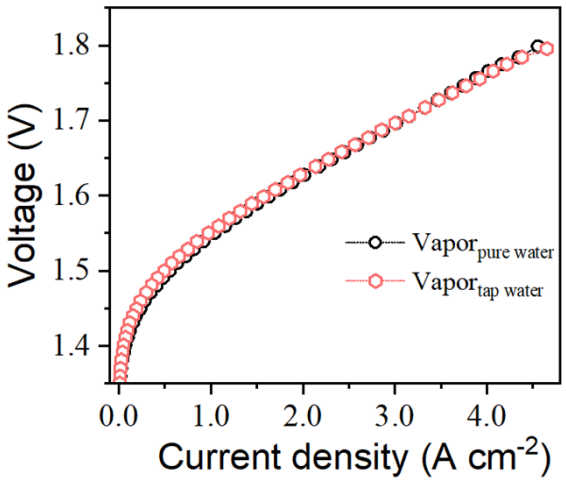

Fig. S21 SVE performance with vapor generated from pure water and tap respectively.

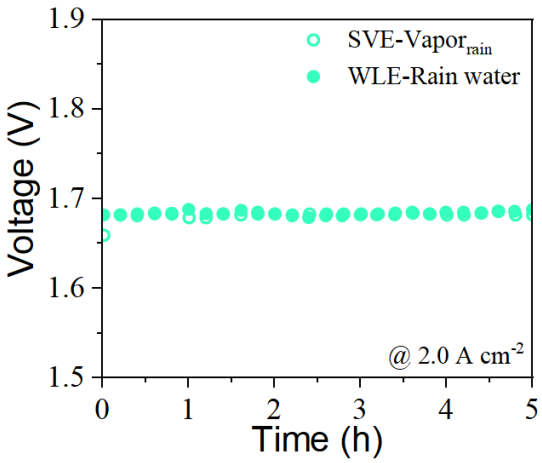

Fig. S22 Sustainability of the SVE dealing with rainwater for operating under 2.0 A cm^{-2} for 5 h compared to the direct rainwater electrolysis. (The rainwater is collected in Perth, Western Australia, and used immediately after collection. Due to its relatively high purity, the

direct electrolysis of rainwater for short-term operation did not cause the failure of the electrolyzer.)

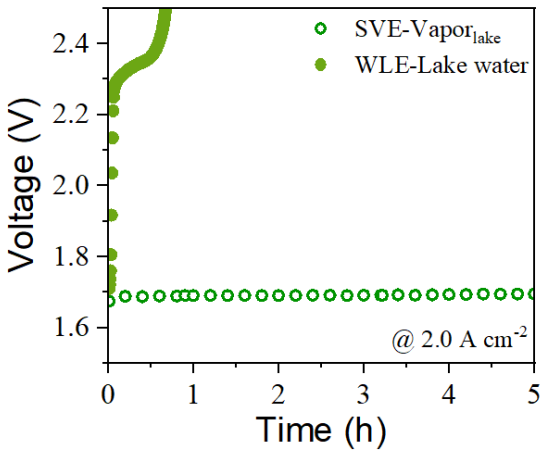

Fig. S23 Sustainability of the SVE dealing with lake water for operating under 2.0 A cm^{-2} for 5 h compared to the direct lake water electrolysis.

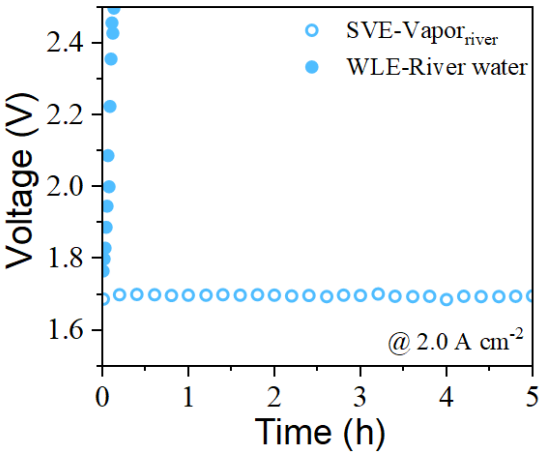

Fig. S24 Sustainability of the SVE dealing with river water for operating under 2.0 A cm^{-2} for 5 h compared to the direct river water electrolysis.

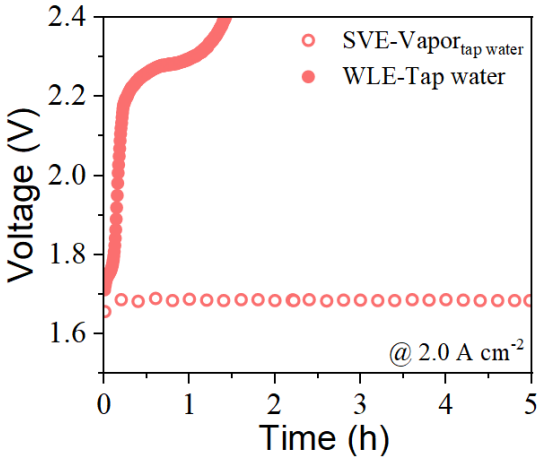

Fig. S25 Sustainability of the SVE dealing with tap water for operating under 2.0 A cm^{-2} for 5 h compared to the direct tap water electrolysis.

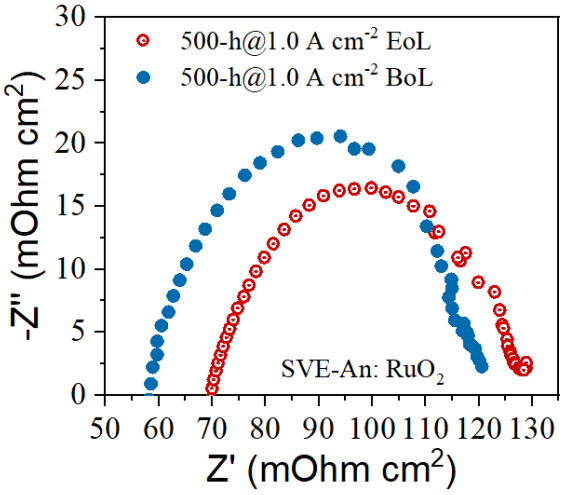

Fig. S26 Nyquist plots from galvanostatic-EIS measurements at 2.5 A of the 2 × 2 cm^2 SVE with RuO_2-based anode before (BoL) and after (EoL) the 500-h stability test at 1.0 A cm^{-2}. (Slight increase of the high frequency resistance observed after the stability test may be due to the increased contact resistance between the components, while the electrode reaction impedance remains almost the same.)

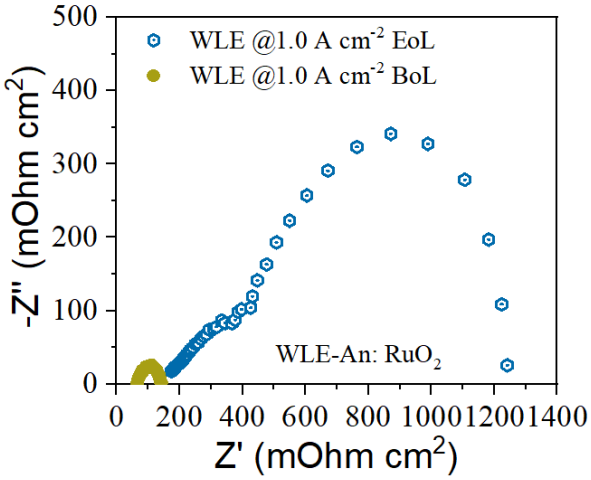

Fig. S27 Nyquist plots from galvanostatic-EIS measurements at 2.5 A of the 2 × 2 cm^2 WLE with RuO_2-based anode before (BoL) and after (EoL) the failure at 1.0 A cm^{-2}. (Both significantly increased high frequency resistance and electrode reaction impedance were observed after the failure of the WLE with RuO_2-based anode, which could be attributed to the loss of RuO_2 that caused the increased contact resistance between the catalyst layer and the gas diffusion layer, as well as the loss of the catalytic sites in the anode.)

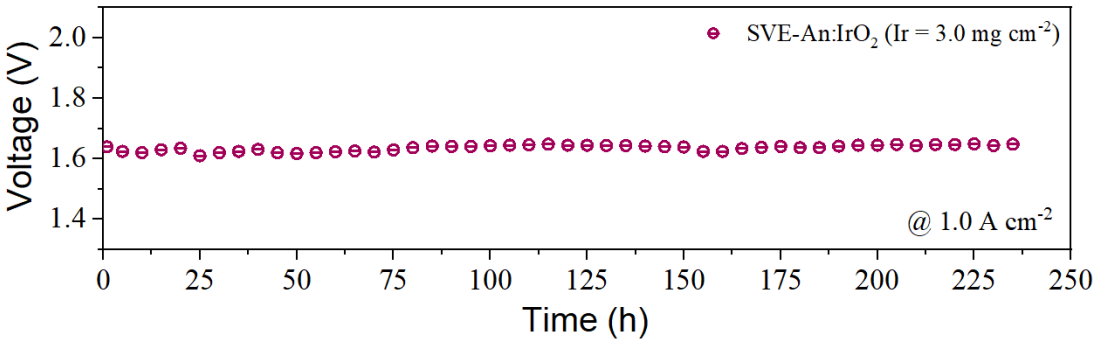

Fig. S28 Stability test for operating the SVE with IrO_2-based anode under 1.0 A cm^{-2} for 235 h (Less than 0.5% performance decrease was observed after the 235-h stability test).

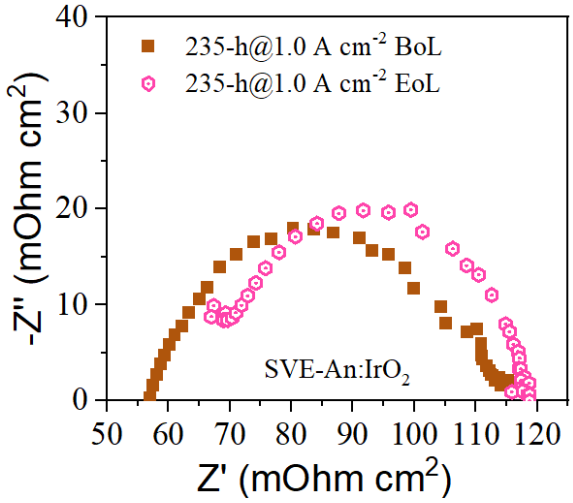

Fig. S29 Nyquist plots obtained from galvanostatic EIS measurements of the 2 × 2 cm^2 SVEs with IrO_2-based anode in operation at 2.5 A applied current before and after the 235-h stability test.

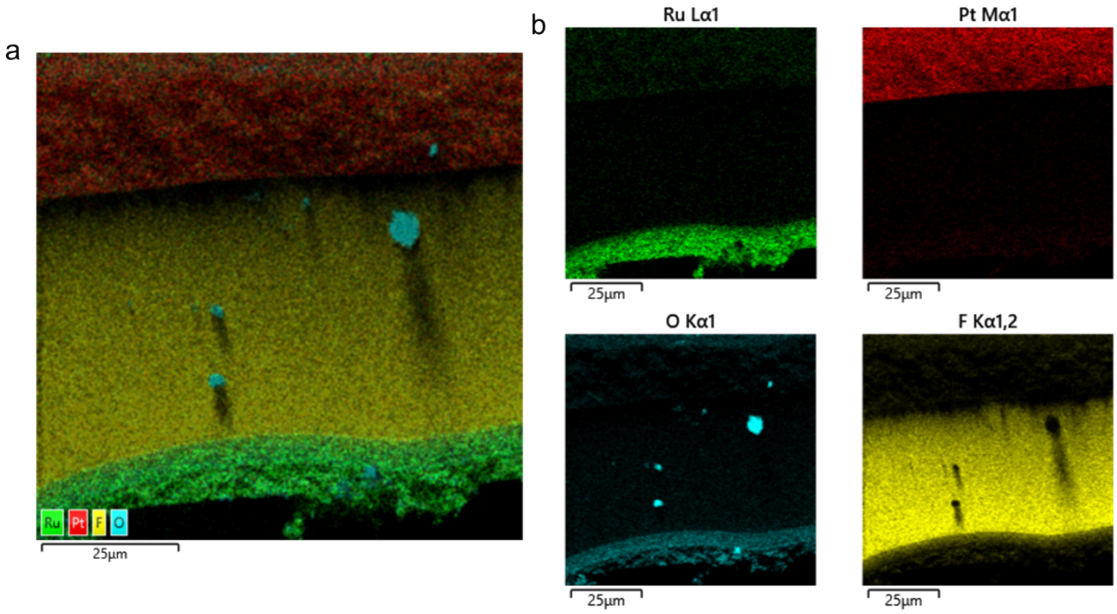

Fig. S30 Scanning electron microscopy (SEM) and energy-dispersive X-ray spectroscopy (EDS) characterizations of the CCM after the SVE stability test under 1.0 A cm^{-2} for 500 h. **a**, Layered EDS mapping and **b**, the individual distribution of O, F, Pt, and Ru elements in the CCM.

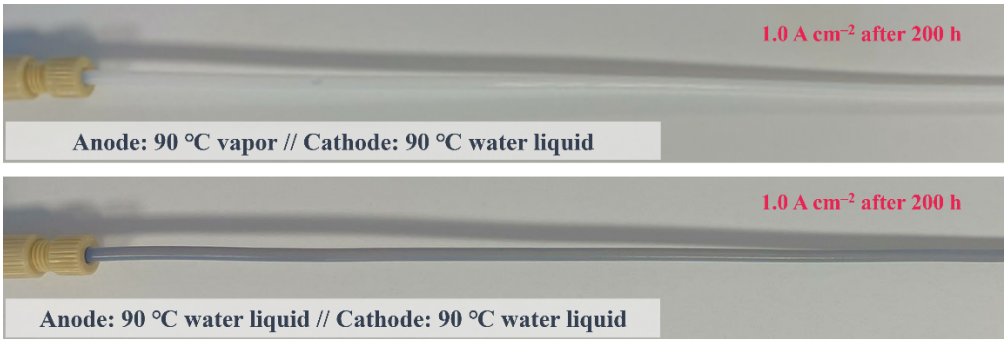

Fig. S31 Images illustrating the attachment of falling catalyst particles at the anode outlet after the stability test conducted at 1.0 A cm^{-2} with vapor and liquid water feeding, respectively.

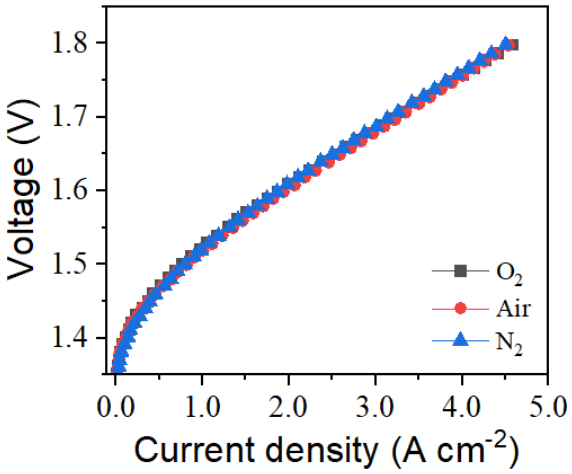

Fig. S32 Performance curves of the SVEs with vapor carried by O_2, N_2, and Air.

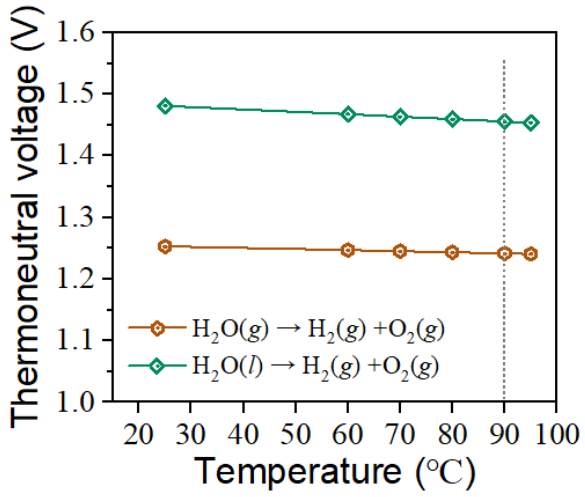

Fig. S33 Theoretical thermoneutral voltage as a function of temperature for water liquid and water vapor electrolysis respectively.

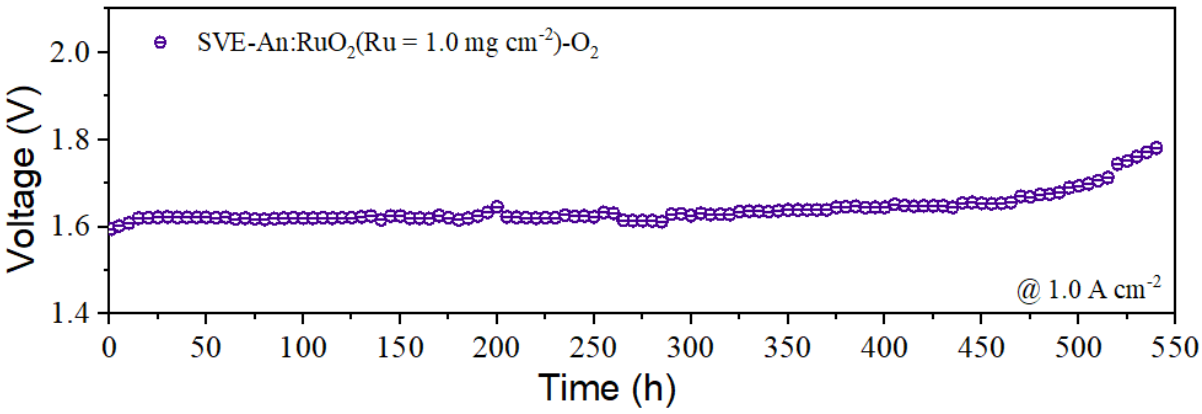

Fig. S34 Stability test for operating the SVE with O_2 as vapor carrier gas under 1.0 A cm^{-2} for 550 h. RuO_2-based anode is used with a Ru loading of 1.0 mg cm^{-2}. (Accelerated performance degradation was observed after 420-h of stable operation, due to the severe corrosion of the unprotected Ti anode plate under oxidative O_2 atmosphere.)

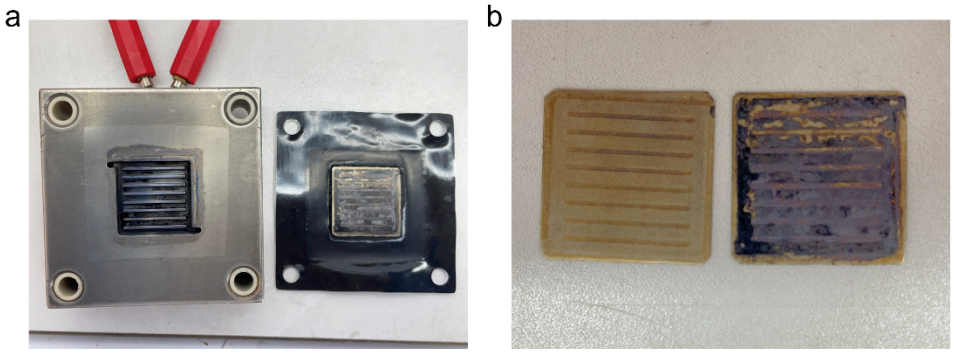

Fig. S35 Pictures showing the corrosion of the anode plate and the gas diffusion layer (GDL) observed after the 550-h stability test of the SVE with O_2 as vapor carrier gas. **a**, The active area of the anode Ti plate without anti-corrosion coating and the GDL side in contact with the anode plate showed serious corrosion after the 550-h stability test. **b**, A comparison of the GDLs after the SVE stability test with N_2 as vapor carrier gas (*left*), and O_2 as vapor carrier gas (*right*).

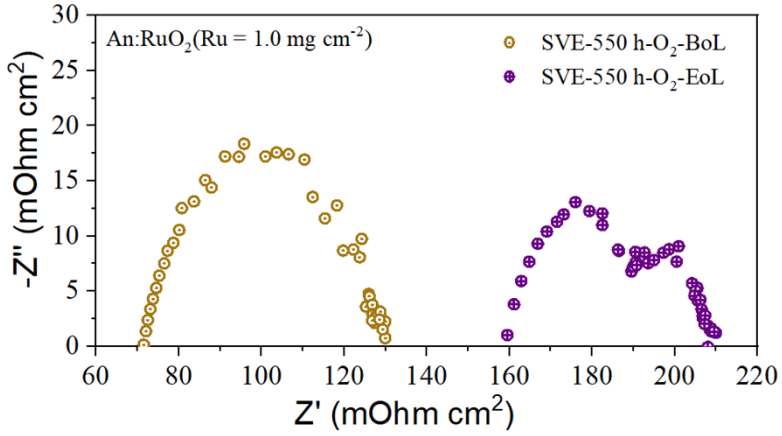

Fig. S36 Nyquist plots obtained from galvanostatic EIS measurements at 2.5 A applied current of the 2 × 2 cm^2 SVEs with O_2 as the carrier gas before and after the 550-h stability test. (The results reflect the performance degradation is mainly due to the greatly increased high frequency resistance after the 550-h operation rather than the electrode reaction impedance, which is in correspondence with the observed phenomena of the anode Ti plate and the GDL corrosion.)

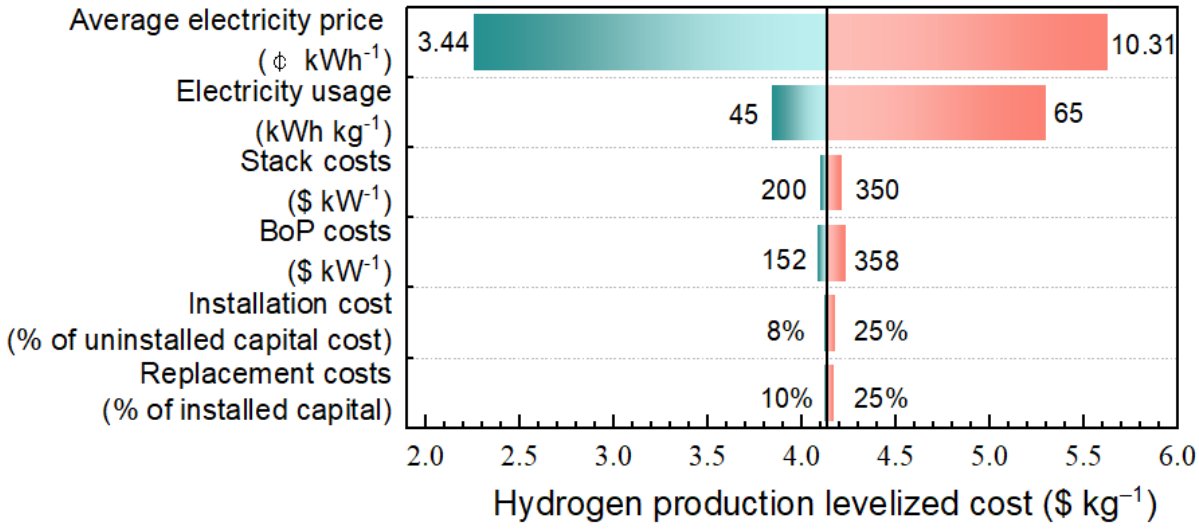

Fig. S37 Tornado chart showing parameter sensitivities for projected hydrogen production levelized cost from SVE technology.

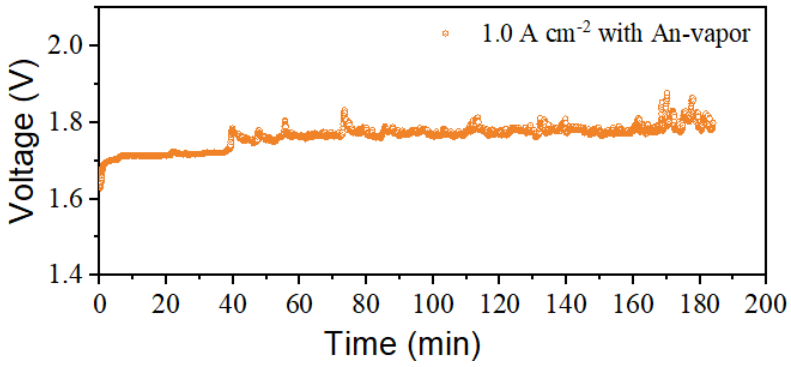

Fig. S38 Stability test for operating the electrolyzer under An-vapor mode (vapor supply to the anode only, with the cathode left free from any supply) at 1.0 A cm^{-2}.

Discussion #1 Thermodynamic calculations of the electrolysis heat and the production of freshwater as a by-product.

We calculated the electrolysis heat (Q_{ex}) involved in water vapor and water liquid electrolysis as below and proposed the co-production of hydrogen and freshwater by taking advantage of the electrolysis heat for the vaporization process. When water electrolysis is operated at the exothermic zone at voltages higher than the thermoneutral voltage (i.e., at 90 °C, for water liquid electrolysis is 1.46 V, for water vapor electrolysis is 1.24 V), the electrolysis heat is released due to the irreversible processes of the reaction as calculated in **Tab. S5**. The SVE theoretically gives off more electrolysis heat for potential re-utilization than the WLE for operating under the same voltage due to the much lower thermoneutral voltage.

Tab. S5 The Q_{ex} for operating the SVE and WLE under different voltages at 90 °C.

Voltage (V)	1.60	1.65	1.70	1.75	1.80
SVE Q_{ex} (kJ mol^{-1})	69.1	78.8	88.4	98.1	107.7
WLE Q_{ex} (kJ mol^{-1})	27.8	37.5	47.1	56.8	66.4

The energy required for the vaporization process includes the part for heating the water source up to designated temperature and the latent heat for water phase transition at that temperature, and additional energy needs to be consumed to heat the carrier gas (e.g., air) to the designated temperature, as shown in **Tab. S6**.

Tab. S6 The energy required for the vaporization process at different temperatures.

Temperature (°C)	60	70	80	90	95
Energy for phase transformation ($\Delta H_{l\rightarrow g,T}$, kJ mol^{-1})	42.48	42.03	41.58	41.12	40.89
Energy for heating water up (Q_T, kJ mol^{-1})	4.54	5.29	6.05	6.80	7.18
Energy for heating Air up ($Q_{T,Air}$, kJ mol^{-1})	1.02	1.31	1.60	1.89	2.04

For the SVE, the electrolysis heat per mole needs to support the generation of 1 mole of water vapor for the electrolysis through the external vaporization process, and the additional part is used for the vaporization to produce n mole of freshwater from the natural water sources after deducting the energy consumption of heating the carrier gas, as expressed below:

$$Q_{ex} = 1.0\left(Q_T + \Delta H_{l\rightarrow g,T}\right) + n_{N2}Q_{T,Air} + n\left(Q_T + \Delta H_{l\rightarrow g,T}\right)$$

Therefore, if we assume to use the electrolysis heat from SVE for the co-production of hydrogen and freshwater, by running the SVE at 90 ℃ at a voltage load of 1.8 V, the production of 1 kg of hydrogen yields an additional generation of 10.68 kg of freshwater.

Discussion #2 Details of techno-economic assessments.

Tab. S7 Input parameters for techno-economic analysis for SVE compared with the referenced PEMWE.[5]

Parameter	The referenced PEMWE	SVE
Cell voltage (V)	1.9	1.8
Stack current density (A cm^{-2})	2.0	4.67
Total uninstalled capital cost ($ kW^{-1})	599	570
Stack capital cost ($ kW^{-1})	342	246
BoP capital cost ($ kW^{-1})	257	224
Total electrical usage (kWh kg^{-1})	55.8	49.0
Stack electrical usage (kWh kg^{-1})	50.4	43.6
BoP electrical usage (kWh kg^{-1})	5.4	5.4
Average electricity price (¢ kWh^{-1})	6.12	6.12
Installation cost (% of uninstalled capital cost)	12%	12%

Stack replacement cost percentage (% of installed capital cost)	15%	15%

Tab. S8 Hydrogen production cost breakdown for SVE compared with the referenced PEMWE.[4]

Component	The referenced PEMWE ($ kg^{-1} H_2)	SVE ($ kg^{-1} H_2)
Capital cost	0.55	0.43
Stack capital cost	0.25	0.18
BoP capital cost	0.18	0.16
Indirect capital cost and replacement cost	0.12	0.09
Feedstock	4.06	3.56
Decommissioning	0.01	0.01
Fixed operations and maintenance (O&M)	0.35	0.35
Variable O&M	0.01	0.01
By-product revenue		-0.23
Hydrogen production cost	4.98	4.13

For capital cost reduction, the Ir loading of 2 mg cm^{-2} in the commercial PEM stack has been substituted with Ru at 1 mg cm^{-2}, halving the loading and reducing the material unit price (Ru cost to 1/10 of Ir cost). Other materials, quantities, preparations, etc., within the PEM stack, all remain consistent with the referenced commercial PEM. Considering the proportion of electrode material cost in the stack cost, the corresponding reduction of hydrogen production cost is calculated to be \$0.088 kg^{-1} H_2.

The mass transfer of water via bubbling enhanced vaporization significantly contributes to the reduction of Balance of Plant (BoP) costs by eliminating the need for water purification equipment. In the reference case, the water management system represents approximately a quarter of the total BoP cost,[4] with water purification devices constituting a significant portion, estimated to be about half of the water management system cost. Calculations indicate a decrease in hydrogen production cost of \$0.031 kg^{-1} H_2 due to this streamlined mass transfer process.

Electricity consumption costs generally represent the largest portion of hydrogen production expenses. Optimizing the electrode to enhance efficiency and decrease power usage stands as

a robust approach to reducing hydrogen production costs. Experimental results showed a reduced electricity consumption of 43.6 kWh kg^{-1} with SVE for H_2 production, whereas commercial PEMWE typically consumes around 50.4 kWh kg^{-1} H_2. The BoP electrical usage is assumed to be consistent with the reference case, standing at 5.4 kWh kg^{-1} H_2. Referring to the same electricity price, the calculations indicate a reduction of \$0.494 kg^{-1} H_2 in hydrogen production cost due to the decreased electricity consumption.

Moreover, the electrolysis heat Q_{ex} generated during SVE operation excluding the part used for vaporization to support electrolysis, also results in excess part, if continue to be used for the evaporation, will produce additional distilled water as a by-product.

During the electrolysis process, the production of 1 mole of H_2 results in the concurrent production of 0.5 moles of O_2, where pure oxygen is also a pivotal industrial raw material. The surplus distilled water and oxygen obtained during the hydrogen production via SVE can be sold to further mitigate the cost of hydrogen. This by-product contribution results in a decrease of \$0.229 kg^{-1} H_2 in the overall hydrogen production cost.

The tornado chart (**Fig. S35**) employs univariate sensitivity to examine the impact of individual parameters on hydrogen cost. The electricity price and its usage are hypothesized to have the greatest impact on the levelized hydrogen cost varying from \$2.26 kg^{-1} to \$5.62 kg^{-1}. This also indicates that the improvement of electrical efficiency through SVE is critical to reducing the hydrogen production cost for practical application.

References

1. van der Pauw, L. J. A method of measuring the resistivity and Hall coefficient on lamellae of arbitrary shape. Philips Technical Review 20, 220-224 (1958).
2. Cox, J. D., Wagman, D. D., & Medvedev, V. A. CODATA key values for thermodynamics. Hemisphere Publishing Corp., New York (1989).
3. Chase, M. W., & National Information Standards Organization (US). NIST-JANAF thermochemical tables. Washington, DC: American Chemical Society. **9**, 1-1951 (1998).
4. James, B., Colella, W., Moton, J., Saur, G., & Ramsden, T. PEM electrolysis H2A production case study documentation (No. NREL/TP-5400-61387). National Renewable Energy Lab (NREL). Golden, CO (United States) (2013).
5. Peterson, D., Vickers, J., & DeSantis, D. Hydrogen production cost from PEM electrolysis-2019. DOE Hydrogen Fuel Cells Program Record **19009**, (2020).